PHYSICAL REVIEW LETTERS **132,** 263803 (2024)

Editors' Suggestion

Hyperbolic Shear Metasurfaces

Enrico M. Renzi,[1,2] Emanuele Galiffi,[1] Xiang Ni,[1,3] and Andrea Alù[1,2,*]
[1]*Photonics Initiative, Advanced Science Research Center, City University of New York, New York, New York 10031, USA*
[2]*Physics Program, The Graduate Center, City University of New York, New York, New York 10026, USA*
[3]*School of Physics, Central South University, Changsha, Hunan 410083, China*

(Received 12 January 2024; accepted 22 May 2024; published 28 June 2024)

Polar dielectrics with low crystal symmetry and sharp phonon resonances can support hyperbolic shear polaritons, which are highly confined surface modes with frequency-dependent optical axes and asymmetric dissipation features. So far, these modes have been observed only in bulk natural materials at midinfrared frequencies, with properties limited by available crystal geometries and phonon resonance strength. Here, we introduce hyperbolic shear metasurfaces, which are ultrathin engineered surfaces supporting hyperbolic surface modes with symmetry-tailored axial dispersion and loss redistribution that can maximally enhance light-matter interactions. By engineering effective shear phenomena in these engineered surfaces, we demonstrate geometry-controlled, ultraconfined, low-loss hyperbolic surface waves with broadband Purcell enhancements applicable across a broad range of the electromagnetic spectrum.

DOI: 10.1103/PhysRevLett.132.263803

Hyperbolic waves emerge in materials featuring extreme optical anisotropy, with opposite signs of the real part of permittivity for orthogonal orientations of the electric field. These waves offer a powerful platform for nanophotonics, thanks to the open topology of their dispersion contours, which asymptotically stretch in momentum space, enabling subdiffractional light confinement combined with directional, raylike propagation [1–7]. In turn, these features enhance the spontaneous emission rate of localized optical sources over broad bandwidths. While hyperbolic wave propagation has been originally explored in the context of metamaterials [3,7,8], it can also be found in natural materials, in particular in polar Van der Waals dielectrics [9–12] and other low-symmetry polar crystals [13–17], which naturally exhibit extreme optical anisotropy associated with directional phonon resonances, leading to hyperbolic phonon polaritons. These hybrid light-matter quasiparticles arise within the Reststrahlen frequency band, within which one component of the permittivity tensor is negative, while the orthogonal one remains positive. While appealing because of their broad availability and lack of nanofabrication requirements, natural hyperbolic materials are restricted to specific frequency ranges in the midinfrared regime [12,14,16].

Whether natural or engineered, bulk hyperbolic waves suffer from dissipation, and their light-matter interactions are hindered by material loss or metamaterial granularity [18]. By contrast, *hyperbolic metasurfaces* [19–21], characterized by highly directional in-plane resonances combined with subwavelength thickness, support effective Reststrahlen bands for surface waves, leading to a reduced impact of material loss and easier access to the fields, since these modes live at the interface with air. These metasurfaces have been implemented across a wide range of frequencies, with exciting prospects for enhanced surface-wave manipulation and broadband interactions with localized emitters close to the surface [11,19,22–25].

Recently, a new family of bulk and surface hyperbolic phonon polaritons was unveiled in monoclinic polar crystals, known as *hyperbolic shear phonon polaritons* [14,15,17]. The nonorthorhombic lattice is associated with directional detuned resonances that are not orthogonal. Within the Reststrahlen band, hyperbolic modes can emerge also in this skewed lattice, but in contrast with conventional hyperbolic polaritons, these modes feature a peculiar rotation of their optical axis with frequency (axial dispersion) and an asymmetric distribution of losses in the different branches of the hyperbolic isofrequency contours (IFCs), driven by microscopic shear phenomena. These features endow hyperbolic shear polaritons with even stronger directionality and field confinement than conventional hyperbolic waves. In turn, shear phonon polaritons are only available in a limited set of natural materials with low crystal symmetry. Consequently, their observation has so far been limited to a nonoptimal subset of possible lattice symmetries and phonon responses.

Here, we introduce and explore *hyperbolic shear metasurfaces*, which are structured surfaces engineered to support hyperbolic surface modes experiencing effective shear phenomena. By optimally breaking the in-plane symmetry of the metasurface, we induce strong axial dispersion and loss redistribution. In turn, this enables directional wave propagation stemming from the intrinsic broken symmetry of the modal dispersion rather than being

© 2024 American Physical Society

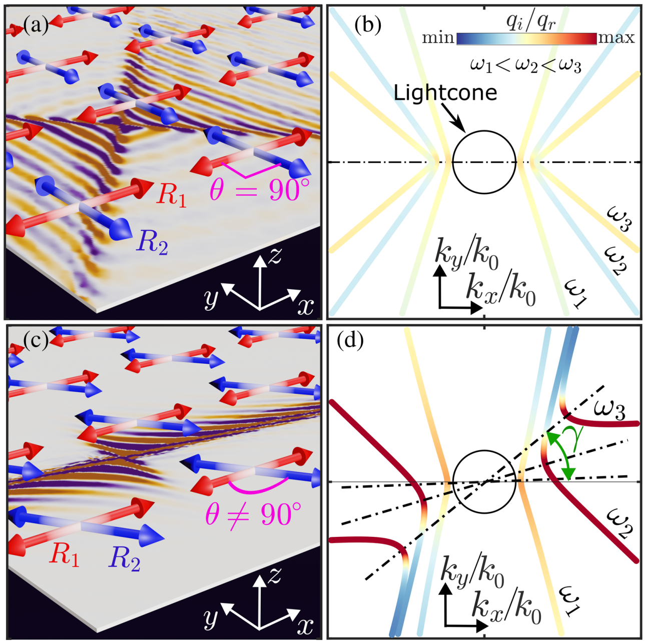

FIG. 1. Axial dispersion and loss redistribution in hyperbolic shear metasurfaces. (a) A metasurface composed of orthogonal detuned resonators supporting (b) hybrid transverse magnetic surface modes with hyperbolic IFCs, featuring nondispersive optical axes (dash-dotted line) and symmetric damping (color map). (c) By rotating the resonators, (d) the optical axis (dot-dashed lines) becomes frequency dispersive, featuring a rotation by an angle $\gamma(\omega, \theta)$ (green) relative to the k_x axis, and the loss becomes asymmetric between the arms of the hyperbolic IFCs (calculated for $\theta = 60^\circ$ and the angular frequencies $\Omega_1 < \omega_i < \Omega_2$, $i = 1, 2, 3$).

induced by the excitation [7,26] or by slanted boundaries [27,28]. We show that the shear response can be tuned and optimized by rotating the relative angle between detuned directional in-plane resonances, leading to enhanced light-matter interactions and exotic propagation features compared to hyperbolic metasurfaces composed of the same underlying elements but in a higher-symmetry configuration.

Consider a metasurface formed by a subwavelength array of detuned dipolar resonators [Fig. 1], placed in free space on the $z = 0$ plane. In the long-wavelength limit, the optical response can be described by the 2×2 homogenized sheet conductivity tensor

$$\hat{\sigma} = \begin{pmatrix} \sigma_1 + \sigma_2 \cos^2(\theta) & -\sigma_2 \sin(\theta)\cos(\theta) \\ -\sigma_2 \sin(\theta)\cos(\theta) & \sigma_2 \sin^2(\theta) \end{pmatrix}, \quad (1)$$

where σ_1 and σ_2 are the effective complex conductivities associated with the two sets of dipolar resonators R_1 and R_2, which in Eq. (1) are assumed to be respectively oriented along the x axis and at an angle θ from it, such that $\hat{\sigma} = \sigma_1 \hat{x} \otimes \hat{x} + \sigma_2 \hat{R}(\theta)(\hat{x} \otimes \hat{x})(\theta)\hat{R}^{-1}$, where $\hat{R}$ is a rotation matrix. The scalar response of each resonator is described by a Lorentzian dispersion $\sigma_j(\omega) = i\sigma_0 N_j \omega^2 / (\omega^2 - \Omega_j^2 + i\omega\Gamma_j)$, where $j = 1, 2$, consistent with the dispersion of polaritonic crystals [16]. Without loss of generality, we assume that the two resonators feature equal loss rates $\Gamma_2 = \Gamma_1$, detuned resonance frequencies Ω_1 and $\Omega_2 = 2\Omega_1$, and oscillator strengths N_1 and $N_2 = N_1/2$. The propagation of surface waves over such an impedance sheet obeys the dispersion relation [29]

$$k_x^2 \sigma_1 + (k_x \cos\theta - k_y \sin\theta)^2 \sigma_2 - k_0^2(\sigma_1 + \sigma_2) = 2k_0 k_z \left(1 + \frac{1}{4}\sigma_1\sigma_2 \sin^2\theta\right). \quad (2)$$

For orthogonal resonators, $\theta = 90^\circ$ [Fig. 1(a)], the metasurface is uniaxial, described by a diagonal conductivity tensor $\mathrm{diag}(\sigma_1, \sigma_2)$. Hyperbolic surface waves are supported when $\Im[\sigma_1] > 0$ and $\Im[\sigma_2] < 0$ [19], within the effective Reststrahlen band of the homogenized surface $\Omega_1 < \omega < \Omega_2$. In this regime, the metasurface features tightly confined, highly directional hybrid transverse magnetic modes with hyperbolic IFCs. The aperture angle of the hyperbolas varies with frequency, while the optical axes are aligned with the orthogonal resonators [Fig. 1(b)]. The IFCs are highly symmetric, and even in the case of asymmetric damping rates in the two resonators ($\Re[\sigma_1] \neq 0 \neq \Re[\sigma_2]$) the four hyperbolic branches feature the same absorption features [19,22,25].

Effective shear phenomena are introduced by rotating R_2 with respect to R_1 [Fig. 1(c)]. In this scenario, $\hat{\sigma}$ acquires nonzero off-diagonal components, coupling the two polarization responses. Remarkably, this metasurface still supports hyperbolic surface waves in its Reststrahlen band, defined as the frequency range for which the two eigenvalues of the Hermitian part of $\hat{\sigma}$ have opposite signs. The symmetry axes of the hyperbolic IFCs are aligned with the reference system that diagonalizes this tensor at any given frequency. Given the nonorthogonality and detuning of the underlying resonators, the hyperbolas rotate with frequency, leading to *axial dispersion*, i.e., a frequency-dependent rotation of the IFCs by the angle $\gamma(\omega, \theta)$ [Fig. 1(d)]. Here we choose $\omega_1 = 1.2\Omega_1$, $\omega_2 = 1.6\Omega_1$ and $\omega_3 = 1.8\Omega_1$. This rotation is quantified by the angle subtended by the k_x axis and the symmetry axis of the hyperbolic IFCs [14,29],

$$\gamma(\omega, \theta) = -\frac{1}{2}\tan^{-1}\left(\frac{\Im[\sigma_2]\sin 2\theta}{\Im[\sigma_1] - \Im[\sigma_2]\cos(2\theta)}\right). \quad (3)$$

Moreover, in contrast to the orthogonal scenario, the loss is distributed asymmetrically across the optical axes. This is to be expected since loss is associated with the resonator polarization directions, and in this nonorthogonal scenario the electric field polarizations more aligned with the resonators (on two of the four hyperbolic branches) experience larger losses than the other two, which support electric fields

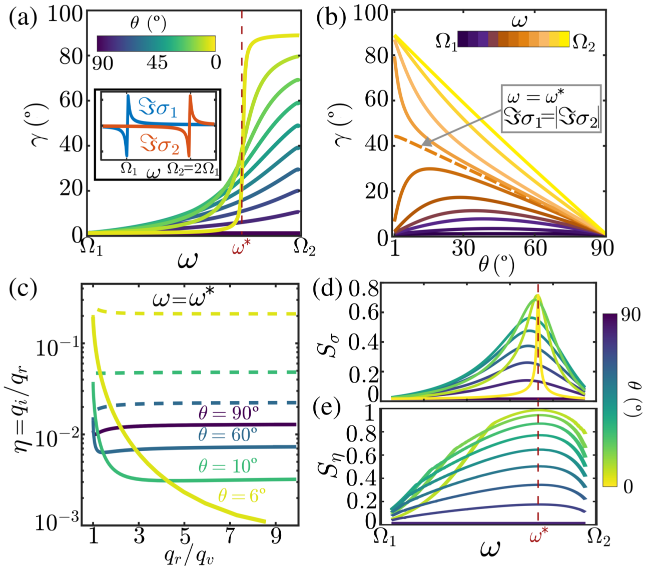

FIG. 2. Axial dispersion and loss redistribution. (a) Dispersion of the optical axis angle $\gamma(\omega, \theta)$. Small twist angles θ (color map) narrow most of the dispersion around the critical frequency ω^*, at which $\Im[\sigma_1] = -\Im[\sigma_2]$. The inset shows the dispersion of the reactive conductivity of R_1 and R_2 within the Reststrahlen band. (b) If $\omega < \omega^*$ (color map), R_1 dominates, and $\gamma(\omega, \theta)$ reaches a maximum before turning back to zero as θ increases. For $\omega > \omega^*$, R_2 is dominant, and the rotation angle varies monotonically with θ. (c) Loss redistribution between the hyperbolic arms as the rotation angle $\theta = (90°, 60°, 10°, 6°)$ is varied. The damping factor η increases in the lossier branches (dashed lines) and decreases in the longer-lived branches (solid lines) as the resonators become less orthogonal, stemming from the IFC vertices located at $q_r = q_v$. Both figures of merit for the degree of loss asymmetry (d) S_σ and (e) S_η peak at the critical frequency ω^*.

less parallel to the resonators and hence less impacted by dissipation. In Fig. 1(d), we quantify the damping factor $\eta = q_i/q_r$ for each point on the IFCs (color map), where q_r (q_i) is the real (imaginary) component of the in-plane wave vector $\mathbf{q} = \mathbf{q}_r + \mathbf{q}_i$ of the surface mode.

Figure 2(a) shows the dispersion of $\gamma(\omega, \theta)$, which grows monotonically with frequency within the effective Reststrahlen band, going from being aligned to R_1 ($\gamma = 0$ at Ω_1) to a larger value at Ω_2. Its evolution corresponds to a counterclockwise rotation of the contours in momentum space. As the resonators become less and less orthogonal, the axial dispersion in Fig. 2(a) steepens, most sharply in the proximity of the *critical frequency* ω^*, for which $\Im[\sigma_1] = -\Im[\sigma_2]$, i.e., the two resonators support a combined resonance as they exhibit equal and opposite reactance, yielding extreme axial dispersion in the presence of effective shear. Figure 2(b) explicitly plots $\gamma(\omega, \theta)$ at the critical frequency, demonstrating how the angle between R_1 and R_2 may be used to dramatically tailor the orientation of the hyperbolic axes. For frequencies closer to the two resonances, the rotation is dominated by one of the resonators. For $\omega < \omega^*$, this manifests in the appearance of a frequency-dependent and controllable turning point beyond which the rotation angle $\gamma(\omega, \theta)$ reverts to zero, bringing the symmetry axis of the IFC parallel to R_1 [29]. Interestingly, at the critical frequency [dashed orange line in Fig. 2(b)] $\gamma(\omega, \theta)$ varies linearly with the rotation angle, ranging between 0 and $\pi/4$. Finally, for $\omega > \omega^*$, R_2 dominates, and $\gamma(\omega, \theta)$ decreases monotonically from $\pi/2$ to 0 following the rotation of R_2 [orange to yellow lines in Fig. 2(b)].

The effective shear phenomena driving axial dispersion are also responsible for loss redistribution between the hyperbolic branches [Fig. 1(d)], increasing the absorption in two of them while enhancing propagation for the other two. This feature produces two surprising effects: given two resonator lattices R_1 and R_2, rotation-induced shear boosts light confinement and propagation length by lowering the impact of loss for two hyperbolic branches, and it enhances the overall directionality of hyperbolic wave propagation. These effects arise throughout the entire Reststrahlen band. To quantitatively explore shear-driven loss redistribution, in Fig. 2(c) we plot the damping factor $\eta = q_i/q_r$ as a function of the normalized in-plane momentum q_r/q_v, where $q_v(\omega^*, \theta)$ is the vertex of the hyperbolic IFC [see inset in Fig. 4(a)] at the critical frequency ω^*. Dashed and solid lines respectively denote the high- and low-loss branches of the same hyperbolic IFC. For orthogonal resonators (purple line), the hyperbolas are symmetric, and the loss in the two resonators equally impacts states that are related to each other by inversion with respect to one of the optical axes. As θ decreases and the resonators become more parallel (light blue to yellow lines), the fixed amount of loss in the resonators is heavily redistributed, making two of the branches increasingly lossier, while freeing the other two as the modes depart from the hyperbola vertex at $q_r = q_v$.

Losses are associated with the non-Hermitian (real) part of $\hat{\sigma}$, whose nondiagonal entries are generally nonzero even after rotating the reference frame by the angle $\gamma(\omega, \theta)$ that diagonalizes the Hermitian part. These off-diagonal non-Hermitian components of $\hat{\sigma}$ quantify the effective shear in the metasurface, whose macroscopic effect is loss redistribution. As a consequence, we can define $S_\sigma(\omega, \theta) = \Re[\hat{\sigma}'_{xy}]/\sqrt{\Re[\hat{\sigma}'_{xx}]^2 + \Re[\hat{\sigma}'_{yy}]^2}$ as a measure of the metasurface shear [29,32]: for $S_\sigma = 0$ we expect perfectly symmetric hyperbolas, corresponding to orthogonal resonators, while at the other extreme $S_\sigma = 1$ supports maximum loss asymmetry. Figure 2(d) shows $S_\sigma(\omega, \theta)$ as a function of frequency and rotation angle, with increasing shear as the angle between resonators is reduced and as we approach the critical frequency.

The definition of $S_\sigma(\omega, \theta)$ does not refer to the specific wave propagation problem at hand, since it does not involve the boundary conditions, and it is therefore agnostic to the specific dispersion relation of the eigenmodes of interest. Its expression measures the general degree of

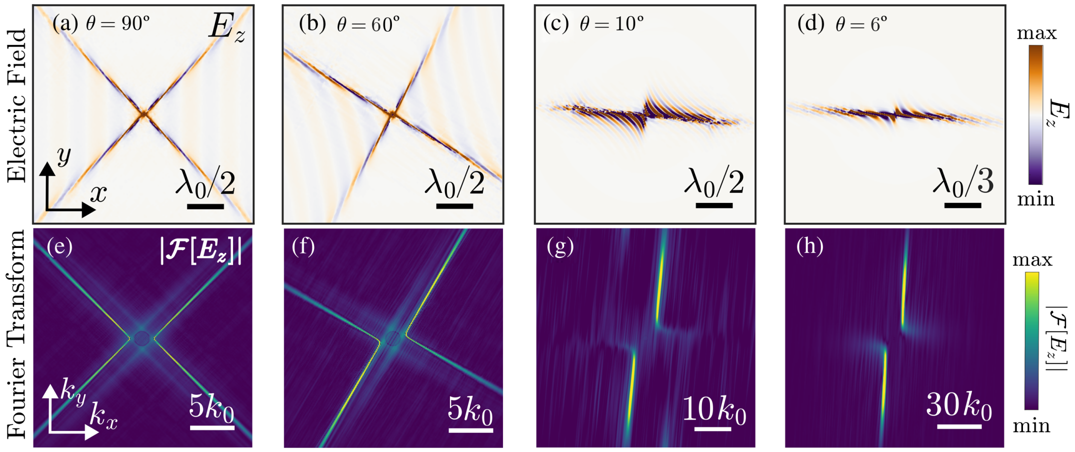

FIG. 3. Near-field excitation of hyperbolic shear surface waves by a localized emitter. Surface waves excited by a z-oriented electric point dipole placed at a distance $d_e = \lambda^*/217$ from the metasurface. (a) For $\theta = 90°$, normal electric field (E_z) and (e) its Fourier spectrum $|\mathrm{F}[E_z]|$ for excitation from a localized emitter. As the rotation angle between the same resonators varies [panels (b),(c)], axial dispersion and asymmetric spectra emerge [panels (f),(g)] showing the impact of shear. Remarkably, in (d),(h) highly confined modes are observed for small rotation angles, exhibiting extraordinarily long-lived propagation enhanced by up to 2 orders of magnitude compared to orthogonal case, despite their tight confinement. Here, $\Omega_1 = \Omega_2/2 = 5$ GHz, $\gamma_1 = \gamma_2 = 0.02\ \Omega_1$, $N_1 = 2N_2 = 1$, and $\omega = \omega^* = 1.733\ \Omega_1$. These parameters match those experimentally used in recent metasurface experiments [21,24].

"electromagnetic asymmetry" of the metasurface and provides an indication of the choice of parameters that maximize it. We can also introduce a quantitative measure of the modal asymmetry $S_\eta(\omega, \theta) = (\eta_+ - \eta_-)/(\eta_+ + \eta_-)$, shown in Fig. 2(e), which explicitly quantifies the loss redistribution by measuring the degree of loss asymmetry in the surface eigenmodes. We evaluate the damping factors η_+ and η_- for mirror-symmetric in-plane momenta located on the bright and dark branches of the IFCs in the limit of large q_r, for which q_i/q_r saturates [29]. Both metrics show a similar dependence on frequency and twist angle, and peak at the critical frequency for small twist angles, i.e., nearly parallel resonators.

Figures 3(a)–3(h) show the spatial distribution of E_z and the associated Fourier spectrum $|\mathrm{F}[E_z]|$ for surface waves launched by a z-oriented electric point dipole emitter placed above the metasurface at distance $\lambda^*/217$ as we vary θ, where $\lambda^* = 2\pi c_0/\omega^*$. We show the results for the critical frequency ω^*, at which the impact of effective shear is strongest. In the case of orthogonal resonators [Figs. 3(a) and 3(e)], the waves propagate symmetrically with respect to the optical axes, aligned with the resonators. As the orthogonality is broken [Figs. 3(b) and 3(c)] the hyperbolic wavefronts rotate and the loss is redistributed, dampening two of the four raylike beams. The lower loss branches experience further field confinement, as they access larger momenta [Fig. 3(c)]. By comparing Fig. 3(e) with Figs. 3(f) and 3(g), the extreme propagation asymmetry and enhanced directionality become apparent. We stress that in the different scenarios we are preserving the same underlying microstructure of the metasurface, i.e., the same features for R_1 and R_2, and the dramatic change in dispersion is only associated with the rotation between them.

Figure 4(a) shows the minimum momentum $q_v = |\vec{q}_v|$ of the hyperbolic IFCs, found at the IFC vertex (purple arrow in the inset), as we vary frequency and rotation angle θ. As the frequency approaches Ω_2 and θ decreases, deeply subdiffractional propagation is achieved as a byproduct of effective shear (see Ref. [29] for further details). As a result of the lower loss and stronger field confinement, light-matter interactions are expected to be largely enhanced. Figure 4(b) shows the enhancement of the Purcell factor [25,33,34] for a z-oriented electric point dipole placed at a distance $d_e = \lambda^*/217$ above the metasurface (inset). Compared to the orthogonal scenario (purple line), the broken symmetry produces a strong broadband enhancement of the emission rate (blue to yellow lines). This effect is consistent with the enhancement of E_z in

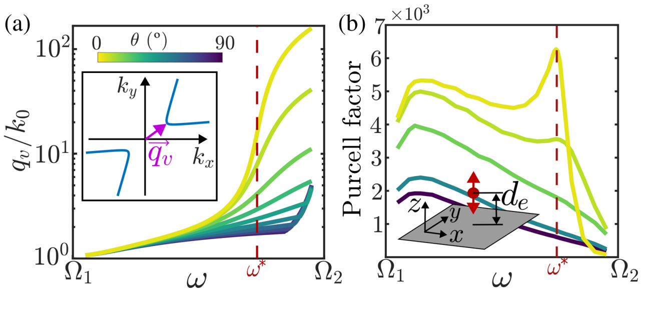

FIG. 4. Induced confinement and spontaneous emission rate enhancement for multiple angles between resonators. (a) Minimum wave number supported by the metasurface q_v at the hyperbola vertex (purple arrow in the inset). (b) Mode confinement and increased lifetime produce a rotation-induced broadband spontaneous emission rate enhancement for a z-oriented electric dipole emitter placed at distance $d_e = \lambda^*/217$ from the metasurface.

Figs. 3(a)–3(d) as θ decreases. For small angles θ between the two resonators, the Purcell factor shows a broad enhancement across the entire Reststrahlen band, with a maximum at $\omega \approx \omega^*$.

In this Letter, we introduced hyperbolic shear metasurfaces that support effective shear phenomena for hyperbolic surface waves, induced by tailoring the angle between detuned directional resonances. Through these effects, we can tailor the directionality and boost the lifetime and Purcell factor of hyperbolic surface waves over tunable bandwidths, achieving extreme control over their propagation and dissipation features. Our work establishes a paradigm that leverages broken symmetries to realize low-loss, ultraconfined, and highly directional surface wave propagation. The phenomena demonstrated may be applied to a wide range of frequencies. These metasurfaces may be realized at radio frequency using a twisted bilayer of detuned resonators [24,35] or in optics using asymmetric V-shaped resonator metaunits [36]. The rational control achieved through the rotational degree of freedom implies that, through tailored optical pumps and nonlinearities, it may be possible to dynamically tune the effective shear in hyperbolic metasurfaces, thus enabling large tunability in real time. These tools may lead to time-dependent axial dispersion and loss redistribution, as well as opportunities for pulse shaping and multiplexing.

The authors thank Simon Yves for the fruitful discussions. This work was supported by the Office of Naval Research and the Simons Foundation. E. G. acknowledges funding from the Simons Foundation through a Junior Fellowship of the Simons Society of Fellows (855344, EG).

---

[*] Corresponding author: aalu@gc.cuny.edu

[1] D. R. Smith and D. Schurig, Phys. Rev. Lett. **90**, 077405 (2003).

[2] H. N. S. Krishnamoorthy, Z. Jacob, E. Narimanov, I. Kretzschmar, and V. M. Menon, Science **336**, 205 (2012).

[3] A. Poddubny, I. Iorsh, P. Belov, and Y. Kivshar, Nat. Photonics **7**, 948 (2013).

[4] V. P. Drachev, V. A. Podolskiy, and A. V. Kildishev, Opt. Express **21**, 15048 (2013).

[5] Z. Liu, H. Lee, Y. Xiong, C. Sun, and X. Zhang, Science **315**, 1686 (2007).

[6] D. Lu, J. J. Kan, E. E. Fullerton, and Z. Liu, Nat. Nanotechnol. **9**, 48 (2014).

[7] P. V. Kapitanova, P. Ginzburg, F. J. Rodríguez-Fortuño, D. S. Filonov, P. M. Voroshilov, P. A. Belov, A. N. Poddubny, Y. S. Kivshar, G. A. Wurtz, and A. V. Zayats, Nat. Commun. **5**, 3226 (2014).

[8] P. Huo, S. Zhang, Y. Liang, Y. Lu, and T. Xu, Adv. Opt. Mater. **7**, 1801616 (2019).

[9] S. Dai, Z. Fei, Q. Ma, A. S. Rodin, M. Wagner, A. S. McLeod, M. K. Liu, W. Gannett, W. Regan, K. Watanabe *et al.*, Science **343**, 1125 (2014).

[10] Z. Zheng, N. Xu, S. L. Oscurato, M. Tamagnone, F. Sun, T. Jiang, Y. Ke, J. Chen, W. Huang, W. L. Wilson *et al.*, Sci. Adv. **5**, eaav8690 (2019).

[11] Q. Zhang, G. Hu, W. Ma, P. Li, A. Krasnok, R. Hillenbrand, A. Alù, and C. Qiu, Nature (London) **597**, 187 (2021).

[12] W. Ma, P. Alonso-González, S. Li, A. Y. Nikitin, J. Yuan, J. Martín-Sánchez, J. Taboada-Gutiérrez, I. Amenabar, P. Li, S. Vélez *et al.*, Nature (London) **562**, 557 (2018).

[13] W. Ma, G. Hu, D. Hu, R. Chen, T. Sun, X. Zhang, Q. Dai, Y. Zeng, A. Alù, C. Qiu *et al.*, Nature (London) **596**, 362 (2021).

[14] N. C. Passler, X. Ni, G. Hu, J. R. Matson, G. Carini, M. Wolf, M. Schubert, A. Alù, J. D. Caldwell, T. G. Folland *et al.*, Nature (London) **602**, 595 (2022).

[15] G. Hu, W. Ma, D. Hu, J. Wu, C. Zheng, K. Liu, X. Zhang, X. Ni, J. Chen, X. Zhang *et al.*, Nat. Nanotechnol. **18**, 64 (2023).

[16] X. Ni, G. Carini, W. Ma, E. M. Renzi, E. Galiffi, S. Wasserroth, M. Wolf, P. Li, A. Paarmann, and A. Alù, Nat. Commun. **14**, 2845 (2023).

[17] J. Matson, S. Wasserroth, X. Ni, M. Obst, K. Diaz-Granados, G. Carini, E. M. Renzi, E. Galiffi, T. G. Folland, L. M. Eng *et al.*, Nat. Commun. **14**, 5240 (2023).

[18] A. N. Poddubny, P. A. Belov, P. Ginzburg, A. V. Zayats, and Y. S. Kivshar, Phys. Rev. B **86**, 035148 (2012).

[19] J. S. Gomez-Diaz, M. Tymchenko, and A. Alù, Phys. Rev. Lett. **114**, 233901 (2015).

[20] O. Y. Yermakov, A. I. Ovcharenko, M. Song, A. A. Bogdanov, I. V. Iorsh, and Y. S. Kivshar, Phys. Rev. B **91**, 235423 (2015).

[21] Y. Yermakov, D. V. Permyakov, F. V. Porubaev, P. A. Dmitriev, A. K. Samusev, I. V. Iorsh, R. Malureanu, A. V. Lavrinenko, and A. A. Bogdanov, Sci. Rep. **8**, 14135 (2018).

[22] P. Li, I. Dolado, F. J. Alfaro-Mozaz, F. Casanova, L. E. Hueso, S. Liu, J. H. Edgar, A. Y. Nikitin, S. Vélez, and R. Hillenbrand, Science **359**, 6378 (2018).

[23] A. A. High, R. C. Devlin, A. Dibos, M. Polking, D. S. Wild, J. Perczel, N. P. de Leon, M. D. Lukin, and H. Park, Nature (London) **522**, 192 (2015).

[24] O. Y. Yermakov, V. Lenets, A. Sayanskiy, J. Baena, E. Martini, S. Glybovski, and S. Maci, Phys. Rev. X **11**, 031038 (2021).

[25] J. S. Gomez-Diaz, M. Tymchenko, and A. Alù, Opt. Mater. Express **5**, 2313 (2015).

[26] F. J. Rodríguez-Fortuño, G. Marino, P. Ginzburg, D. O'Connor, A. Martínez, G. A. Wurtz, and A. V. Zayats, Science **340**, 328 (2013).

[27] Z. Dai, G. Hu, G. Si, Q. Ou, Q. Zhang, S. Balendhran, F. Rahman, B. Y. Zhang, J. Zhen Ou, G. Li *et al.*, Nat. Commun. **11**, 6086 (2020).

[28] I. Deriy, K. Lezhennikova, S. Glybovsky, I. Iorsh, O. Yermakov, M. Song, R. Abdeddaim, S. Enoch, P. Belov, and A. Bogdanov, arXiv:2308.10495.

[29] See Supplemental Material at http://link.aps.org/supplemental/10.1103/PhysRevLett.132.263803 for the derivation of the dispersion equation and rotation angle formula, analysis of mode confinement, derivation of the shear factor, and more details on the Purcell factor enhancement, which includes Refs. [30,31].

[30] H. J. Bilow, IEEE Trans. Antennas Propag. **51**, 2788 (2003).

[31] J. A. Stratton, *Electromagnetic Theory*, IEEE Press Series on Electromagnetic Wave Theory, (John Wiley & Sons, Hoboken, NJ, 2007).

[32] S. Yves, E. Galiffi, X. Ni, E. M. Renzi, and A. Alù, Phys. Rev. X 14, 021031 (2024).

[33] A. Bapat, S. Dixit, Y. Gupta, T. Low, and A. Kumar, Nanophotonics **11**, 2329 (2022).

[34] L. Novotny and B. Hecht, *Principle of Nano-Optics* (Cambridge University Press, Cambridge, England, 2012).

[35] A. Girich, L. Ivzhenko, A. Hrinchenko, S. Tarapov, and O. Yermakov, IEEE Microwave Wireless Technol. Lett. **33**, 367 (2023).

[36] K. Koshelev, S. Lepeshov, M. Liu, A. Bogdanov, and Y. Kivshar, Phys. Rev. Lett. **121**, 193903 (2018).